sustainable chemistry

MDPI

*Article*

# Designing a Photocatalyst: Relationship Between Surface Species and Specific Production of Desired ROS

**Fabrizio E. Viale [1], Verónica R. Elías [1], Tamara B. Benzaquén [1], Gerardo F. Goya [2], Griselda A. Eimer [1] and Gabriel O. Ferrero [1,*]**

[1] Centro de Investigación y Tecnología Química (CITeQ), Universidad Tecnológica Nacional (UTN)—Consejo Nacional de Investigaciones Científicas y Técnicas (CONICET), Maestro Marcelo López esq. Cruz Roja Argentina, Córdoba 5016ZAA, Argentina; fviale@frc.utn.edu.ar (F.E.V.); velias@frc.utn.edu.ar (V.R.E.); tbenzaquen@frc.utn.edu.ar (T.B.B.); geimer@frc.utn.edu.ar (G.A.E.)

[2] Instituto de Nanociencia y Materiales de Aragón (INMA), Universidad de Zaragoza (UNIZAR), C/Mariano Esquillor Gómez s/n, 50018 Zaragoza, Spain; goya@unizar.es

* Correspondence: gferrero@frc.utn.edu.ar

**Abstract**

Bimetallic mesoporous photocatalysts were synthesized via a wet impregnation method using SBA-15 as a support, and characterized by UV–visible diffuse reflectance spectroscopy, low-angle X-ray diffraction and $N_2$ physisorption. Among the tested materials, the Ti/Mn combination exhibited the highest photocatalytic activity in azo dye degradation. To understand this enhanced performance, catalysts with varying Mn loads and calcination ramps were evaluated. Additionally, experiments with radical scavengers (isopropanol, chloroform) and under $N_2$ insufflation were conducted to identify the active radical species. Catalysts prepared with low Mn content and higher calcination ramps showed the greatest activity, which significantly decreased with isopropanol, indicating hydroxyl radicals as the main reactive species. In contrast, samples with higher Mn content and quicker heating displayed reduced activity in the presence of chloroform, suggesting superoxide radical involvement. Spectroscopic analyses (XPS, UV–Vis DRS) revealed that increasing Mn load promotes the formation of $Mn^{2+}$ over $Mn^{4+}$ species and lowers the band gap energy. These findings highlight the direct correlation between synthesis parameters, surface composition and optical properties, providing a strategy for fine-tuning the performance of a photocatalyst.

**Keywords:** heterogeneous photocatalysis; mesoporous silica; manganese; radical scavengers; reactive oxygen species



Academic Editor: Matthew Jones

Received: 9 June 2025
Revised: 17 September 2025
Accepted: 20 September 2025
Published: 23 September 2025

**Citation:** Viale, F.E.; Elías, V.R.; Benzaquén, T.B.; Goya, G.F.; Eimer, G.A.; Ferrero, G.O. Designing a Photocatalyst: Relationship Between Surface Species and Specific Production of Desired ROS. *Sustain. Chem.* **2025**, *6*, 31. https://doi.org/10.3390/suschem6040031



## 1. Introduction

Advanced oxidation processes (AOPs) are a group of emerging techniques aimed at degrading organic pollutants, with the goal of achieving complete mineralization into water and carbon dioxide. These processes have been extensively investigated and applied in various fields in recent years [1,2]. Among these techniques, photocatalytic methods stand out for their high efficiency and ease of implementation in aqueous systems, where the presence of a photocatalyst and light irradiation are sufficient to generate reactive oxygen species (ROS) that drive the degradation of organic compounds. Photocatalysis is promoted by the generation of photoinduced electrons ($e^-$) and holes ($h^+$) on the solid surface of a semiconductor upon irradiation [3]. These $e^-$ and $h^+$ are key in a series of chain redox reactions that yield a number of ROS, mostly hydroxyl ($HO^\bullet$) radicals [4].

Nevertheless, other species, such as singlet oxygen ($O_2{}^1$), hydrogen peroxide ($H_2O_2$) or superoxide anion radical ($O_2{}^{\bullet-}$) are also in this group [3].

The superoxide radical has been largely studied in biological pathways due to its involvement in respiration and immune system processes [5–7], but its role in the degradation of organic substances has been relegated in favor of the study of hydroxyl radical chemistry [8]. Thus, understanding the reactivity of superoxide remains crucial, as its unique chemical properties distinguish it from hydroxyl radicals. Superoxides are unstable species due to their radical nature, but they are less reactive than hydroxyl ones [9,10]. Its chemistry is strongly related to its solvation ability in different media due to its dual state as a radical and as an anion [10]. It is not easy to generate and isolate a radical species, so its chemistry is yet to be fully understood [11]. In addition, due to the short half-life of superoxide anion radicals, their investigation and detection is a critical step in the study of photocatalytic processes. Therefore, it would be highly desirable to apply simple, reproducible, and quick spectrometric methods for its detection [12–14]. Furthermore, $TiO_2$ has been the most popular semiconductor in photocatalysis to produce ROS due to its favorable physicochemical properties and availability [15]. However, the practical application of $TiO_2$ in liquid-based media remains difficult. $TiO_2$ particles are very small and thus hard to recover from a liquid effluent [16,17]. Another issue related to $TiO_2$ is its band gap energy (3.2 eV), limiting its use under $UV_A$-based applications. In order to overcome these challenges, impregnation of $TiO_2$ [17] and other photocatalytic species [18,19] over different supports, as well as development of bimetallic catalysts [20,21] have been applied in previous studies. Moreover, the synergic effect of bi- [22] and polymetallic photocatalysts [23] has been reported. The different $TiO_2$ species formed as a consequence of variable metal loading on Ti-based mesoporous photocatalysts have been studied [22].

Impregnation of $TiO_2$ particles over mesoporous supports such as SBA-15 silica leads to materials with a higher thermal and hydrothermal stability, yielding large surface areas. In addition, modifying synthesis conditions and varying metal loading can be of great significance due to the many different structures that may be developed on the surface. In this regard, the synthesis of solids by means of co-modification of SBA-15 with $TiO_2$ and other metallic species can be crucial to modify their properties as photocatalysts and, therefore, the selectivity toward the different generated ROS.

Several authors have shown that different proportions of metal provide different structures [24,25], while varying calcination rates generate different silica–metal interfaces [26] that modify the catalyst photoactivity. Considering possible metal species to be used, manganese oxides (MnOx) stand out due to their wide availability and multiple possible configurations [27]. Copper oxides (CuOx) are another very versatile group of metallic oxides with large availability that is increasingly studied in association with $TiO_2$ [28–30]. Moreover, cobalt oxides (CoOx) can also strongly enhance the photoactivity of $TiO_2$ in the visible region, and interesting results have been observed for wastewater treatment [31,32].

Based on previously characterized mesoporous materials which showed ability to photogenerate different radical species [33], this research focuses on the development and optimization of mesoporous photocatalysts derived from SBA-15 silicates, modified with titanium and an additional transition metal (Co, Cu, or Mn), individually introduced to produce a series of bimetallic Ti/M catalysts. These materials were synthesized with varying nominal metal loadings and calcination heating rates in order to explore the effect of these parameters on the resulting physicochemical properties, metal–support interactions, and photocatalytic activity. The catalysts were evaluated for their ability to generate reactive oxygen species (ROS) under UV–Vis light and to degrade Acid Orange 7 (AO7), a commonly used azo dye model pollutant. Finally, to make a more exhaustive study of the photocatalytic process and analyze the selectivity towards the formation of

two of the main ROS, $^{\bullet}OH$ and $O_2^{\bullet-}$, reactions were carried out in the presence of specific radical quenchers: isopropanol for $^{\bullet}OH$ [34] and chloroform for $O_2^{\bullet-}$ [35].

## 2. Materials and Methods

### *2.1. Synthesis*

The synthesis followed the same steps as in a previous report [33], with the mesoporous silica support synthesized following the method for SBA-15-type materials [36]. For this synthesis process, Pluronic P123 (Sigma-Aldrich, St. Louis, MO, USA; 100%) was dissolved overnight in aqueous 2M solution HCl (Cicarelli, San Lorenzo, Argentina; 36.5–38%) under stirring at 40 °C. Afterwards, tetraethoxysilane (TEOS) (Sigma-Aldrich, 98%) was added dropwise to the solution and further stirred at the same temperature for 20 h. The as-obtained sol-gel underwent hydrothermal aging at 80 °C for 24 h. The material was then filtered, washed, and dried for 24 h at 60 °C. Finally, the Pluronic P123 surfactant was removed by calcining in a muffle furnace at 500 °C for 8 h, heating at a rate of 1 °C/min.

A portion of the as-obtained mesoporous support was used for characterization techniques. Another three batches of this same material were modified via the wet impregnation method with transition metals Co, Cu, and Mn, using $CuSO_4 \cdot 5H_2O$ (Mallinckrodt, St. Louis, MO, USA; 99%), $CoSO_4 \cdot 7H_2O$ (Sigma-Aldrich, 98%), or $MnSO_4 \cdot H_2O$ (Merck, Darmstadt, Germany; 99%) as precursors, respectively. A nominal load of 10 wt.% of each metal was expected to be achieved by employing properly concentrated aqueous solutions of the aforementioned salts. The three batches were suspended in the respective solutions, and the solvent was removed with a rotovap at 70 °C. After this step, the supports were dried at 90 °C and calcined, heating at a rate of 4 °C/min to a temperature of 500 °C for 5 h.

Afterwards, four different supports (the previously obtained materials and an unmodified silica batch) were impregnated with Ti, with titanium n-butoxide, $Ti(OBu)_4$ (Sigma-Aldrich, 97%) as a metal source in a concentration adequate to reach a fixed nominal load of 20 wt.%. The procedure was the same as in the previous impregnation, but using isopropanol (Sintorgan, Buenos Aires, Argentina; 99.5%) instead of water, removing the solvent with a rotovap at 55 °C. The obtained materials were identified as Ti/Co/M, Ti/Cu/M, Ti/Mn/M, and Ti/M, where "M" represents the mesoporous support.

Once the more photoactive bimetallic catalyst was determined, new batches were prepared by varying the synthesis conditions to tune the reaction selectivity for the production of different possible ROS. Therefore, the same impregnation method previously described was applied to load different nominal metal weights of 2.5, 5, and 10 wt.%, along with a fixed nominal load of 20 wt.% Ti. Moreover, calcination processes with different heating rates (4 and 8 °C/min) were tested because of their influence on the development of different metallic species. The obtained materials were labeled as Ti/[Metal](x)/M R(y), where (x) represents the nominal wt.% of loaded metal and (y) the applied heating rate.

### *2.2. Characterization*

Unmodified and modified mesoporous silicas were characterized via low-angle X-ray diffraction (XRD) through a PANalytical X-Pert Pro instrument with CuK$\alpha$ radiation ($\lambda$ = 1.5418 Å) between 1.2 and 3° 2$\Theta$ angles. Textural properties were characterized through a Micromeritics ASAP 2020 Plus sorption analyzer, using $N_2$ as the sorption gas and with the solid materials degassed at 350 °C. The optical properties of the materials were established via UV–visible diffuse reflectance spectroscopy (UV–Vis DRS), obtained through a Jasco V650 spectrophotometer equipped with an integrating sphere. Metallic species were determined by X-ray photoelectronic spectroscopy (XPS) using a XPS K-Alpha Thermo Scientific instrument equipped with a low-power AlK$\alpha$ X-ray source and

a double-focusing hemispheric analyzer. CasaXPS (Version 2.3.26) software was used for spectra analysis.

### *2.3. Catalytic Experiments*

The photocatalytic experiments were carried out with a stirred batch photoreactor, irradiated over its top. The photoreactor consists of a 25 mL Teflon beaker which is positioned over a magnetic stirrer. The suspension is directly irradiated with a 390 nm UV/Vis LED 30 W lamp installed over a window in a fireproof coating-covered wood platform. The light is distributed between 360 and 420 nm, with a peak at 390 nm. Additionally, the relative radiometric optical power distribution is highly concentrated in this type of design, with at least 90% of the total light output confined within a 55° angle [37,38]. The LED is equipped with a large heat sink in order to avoid temperature increases, as seen in Figure 1. For each of the experiments, 20 mg of modified mesoporous material were suspended in 20 mL (for a catalyst concentration of 1 g/L) of AO7 (Sigma Aldrich, 99.5%) solution (20 ppm). Following a 45 min incubation period in the dark, during which the change in AO7 concentration was negligible—indicating that adsorption/desorption equilibrium had been reached—a sample was collected to determine the initial concentration ($C_0$). The experiment was then initiated by exposing the system to light for 3 h, and the AO7 concentration ($C$) was monitored by measuring the absorbance at 485 nm using a Persee T7DS UV/Vis spectrophotometer. The percentage degradation ($X$) was calculated using the following equation:

$$X = (C_0 - C) \times 100 / C_0$$

where $X$ is the degradation percentage, and $C$ is the AO7 concentration at a given reaction time.

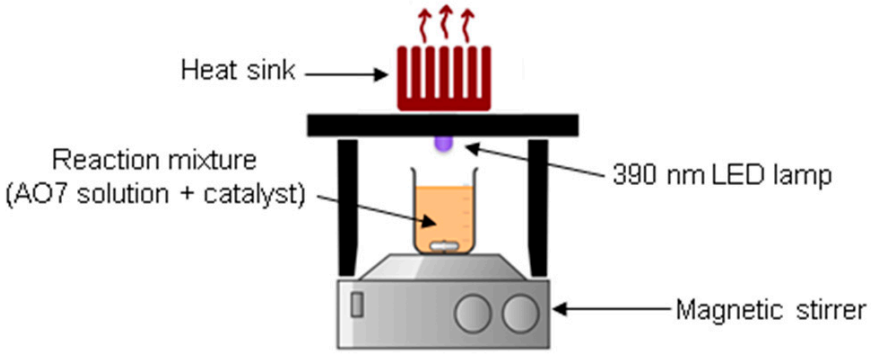


**Figure 1.** Components and disposition of the photoreactor.

A control experiment is presented in Figure S1 (Supplementary Material), in which the concentration of AO7 was monitored under LED lamp irradiation for 3 h. The results show that the concentration remains constant, indicating that photolysis does not occur under these conditions. Finally, reactions in the presence of 8% vol. isopropanol (Sintorgan, 99.5%) or 4% vol. chloroform (Cicarelli, 99%)—used as specific scavengers of hydroxyl or superoxide radicals, respectively—were carried out in order to infer about selectivity towards the possibly involved ROS.

Some ROS were also detected with an Attenuated Total Reflectance–Fourier-Transform Infrared (ATR-FTIR) spectrometer using a Thermo Scientific Nicolet iS10 equipped with a Smart ARK module. This was achieved by placing 3 mL of 1 g/L suspension of photocatalyst in water over the ATR mode ZnSe window. The LED lamp was placed on top of the module, irradiating the suspension. Under these conditions, spectra were recorded at 10 and 30 min.

## 3. Results and Discussion

### *3.1. Characterization of Synthesized Materials*

The low-angle X-ray diffraction (XRD) technique was used to determine whether the synthesized support shows peaks consistent with planes present in SBA-15 mesoporous silicas. Thus, the pattern shown in Figure 2 presents peaks at 1.60 and 1.84°, which can be assigned to the planes (110) and (200), respectively, typical of highly-ordered SBA-15 type materials [36]. The diffractograms of the post-synthesis catalysts (presented in Figure S2, Supplementary Material) show that these peaks remain after metal impregnation, thus the modified silicas retain the mesoporous structure.

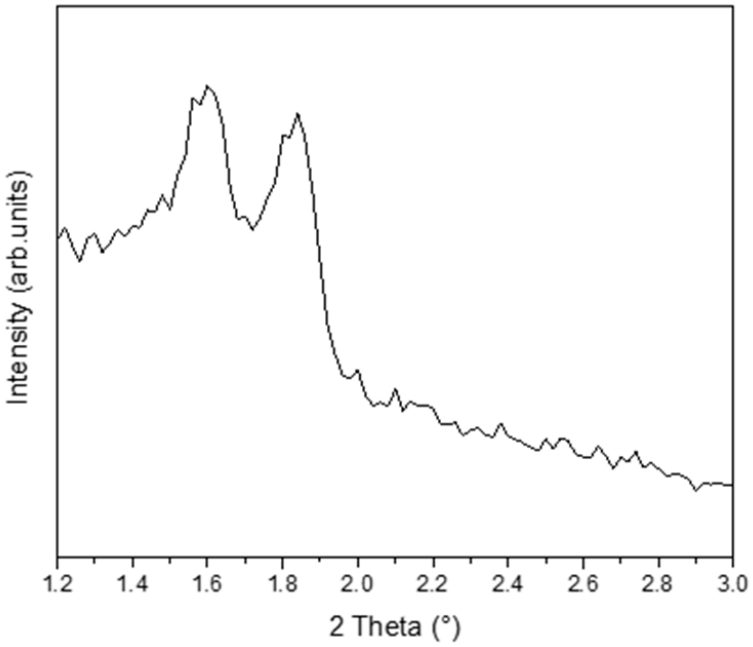


**Figure 2.** Low-angle X-ray diffraction (XRD) pattern of unmodified silica framework.

Figure 3 shows the $N_2$ adsorption–desorption isotherms of bare SBA-15, Ti/M, Ti/Cu/M, Ti/Co/M, and Ti/Mn/M. All of the studied materials exhibit a type IV isotherm, which is typical for mesoporous structures [39]. Unmodified mesoporous support presents a H1 hysteresis loop, which is consistent with that of silicas exhibiting highly-arranged uniform mesopores [39–41]. When the support is modified only with Ti, the material presents a H5 hysteresis loop, a type of loop associated with partially blocked mesopores [39], which has been found in post-synthesis modified SBA-15 materials [42,43]. The bimetallic mesoporous supports exhibit different types of hysteresis loops. Ti/Cu/M presents a H2b type of loop that is associated with pore-blocking phenomena due to a broad size distribution of pore neck widths and a narrow distribution of pore cavity sizes [39,44], which means Cu and Ti species are mainly deposited in the pore end points. This type of distribution has been found in other modified mesoporous supports [45], modified with Ti [46]. Ti/Co/M presents a H2b and H1 hybrid type of hysteresis loop, which is narrower and indicates a smaller distribution of neck widths [39,44]. Meanwhile, Ti/Mn/M presents a H2a type of loop, associated with materials that exhibit a wide distribution of pore body sizes but a narrower distribution of pore neck widths [44], which has been already reported in Zr [47] and polymer-modified [45] mesoporous materials. This distribution signals higher deposition of Mn and Ti species along the mesoporous channels.

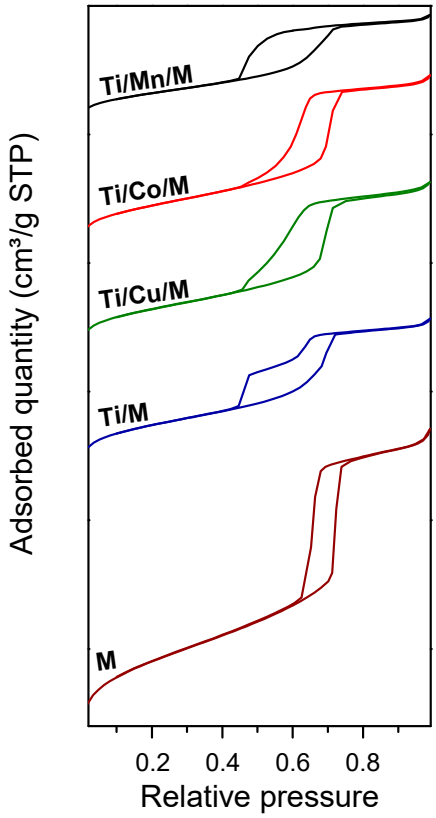


**Figure 3.** $N_2$ adsorption–desorption isotherms for all the mesoporous materials.

Table 1 summarizes the textural properties of the materials, with the Brunauer–Emmett–Teller (BET) specific area, pore volume (PV), and pore diameter (PD) singled out. As it can be seen, bimetallic modification leads to larger presence of Ti along the channels, as Ti/M presents the lowest pore diameter with largely blocked pores, which is consistent with its H5 hysteresis loop. It should also be noted that Ti/Mn/M exhibits a remarkably smaller pore volume and pore diameter than the other bimetallic catalysts did, consistent with a high presence of both metals along the pores, according to its isotherm. Nevertheless, after metallic impregnation, a substantial decrease in pore diameter was observed in all synthetized materials.

**Table 1.** Textural and optical properties of the mesoporous materials.

| Material | $S_{BET}$ ($m^2g^{-1}$) [a] | PD (nm) [b] | PV ($cm^3g^{-1}$) [b] | Eg (eV) [c] |
|---|---|---|---|---|
| M | 816 | 5.8 | 1.03 | --- |
| Ti/M | 485 | 4.6 | 0.52 | 3.51 |
| Ti/Cu/M | 399 | 5.5 | 0.55 | 3.44 |
| Ti/Co/M | 403 | 5.5 | 0.56 | 1.49 |
| Ti/Mn/M | 289 | 4.9 | 0.35 | 3.27 |

[a] Calculated from the linear part of the Brunauer–Emmett–Teller (BET) plot, [b] Estimated by the Barrett–Joyner–Halenda (BJH) formula using the desorption branch from the isotherm, [c] Estimated with the Kubelka–Munk equation as a function of the energy.

The band gap energy (Eg) of the metal-modified photocatalysts was calculated from the UV–Vis DR spectra (Figure S3A, Supplementary Material) using the graphic method based on fitting the Kubelka–Munk (KM) equation as a function of the energy in eV (Figure S3B, Supplementary Material). As can be observed in Table 1, a band gap reduction from 3.51 eV for Ti/M to 3.44 and 3.27 eV for Ti/Cu/M and Ti/Mn/M, respectively, is observed. Meanwhile, for Ti/Co/M, the band gap decreases to 1.49 eV.

### 3.2. Photocatalytic Evaluation of Materials

Figure 4 shows the photocatalytic evaluation of the materials in AO7 removal. As seen in the figure, Ti/Mn/M shows the highest photocatalytic activity, while Ti/Co/M presents the lowest—even lower than that of Ti/M—despite its low band gap energy. There have been multiple studies focusing on the complex mechanisms involving cobalt, which can either enhance photoactivity or suppress it. According to Gonçalves et al. [48], photoactivity is favored when cobalt is present at proportions below 0.5% as a dopant in the catalyst. However, when cobalt content exceeds this threshold, it acts as a recombination center due to the low stability of the $Co^{3+}$ species formed, which markedly decreases photoactivity. This point is in agreement with Pradhan et al. [49], who via PL studies on pure $Co_3O_4$ discovered high signal intensity related to high electron-hole recombination. Meanwhile, Dong et al. [50] evaluated the $Co_3O_4/TiO_2$ bimetallic support and concluded that $Co_3O_4$ exhibits high hole-trapping capability, with electrons falling back to the valence band, transferring photogenerated holes from $TiO_2$ to $Co_3O_4$. Collectively, these findings support the view that cobalt acts as an electron–hole recombination center, thereby reducing photocatalytic efficiency. In the present study, the DRS spectrum of Ti/Co/M (Figure S3A) shows absorption peaks at 484.5 nm and 733 nm, which can be attributed to charge-transfer transitions in $Co_3O_4$. This behavior closely resembles that described in [50], indicating an accelerated recombination of photoexcited electrons and holes [51], along with a low redox potential that limits photocatalytic performance [33,52].

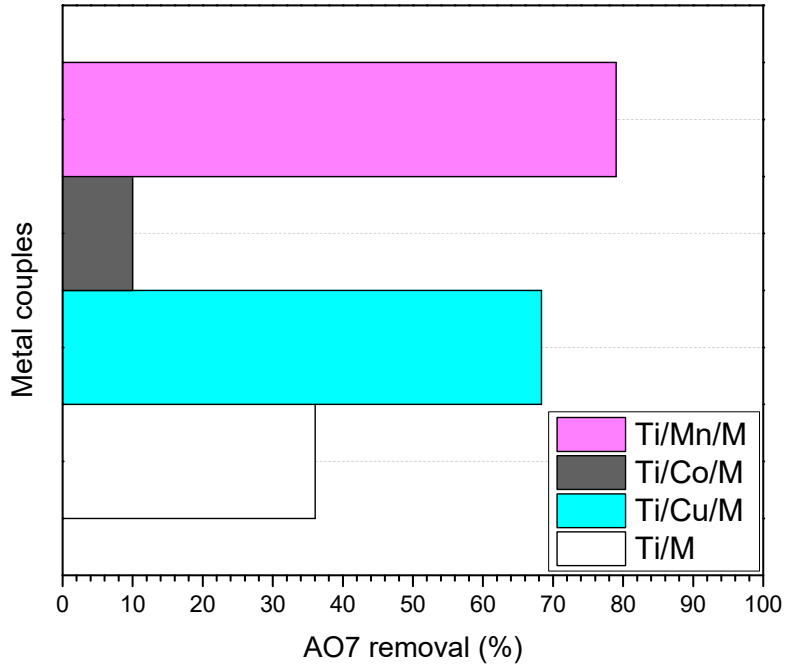


**Figure 4.** AO7 removal via photocatalytic activity of the tested mesoporous materials. Reaction conditions: pH = 5, T = 25 °C, catalyst concentration = 1 g/L, rotational speed = 600 rpm.

These results, compared with previous studies involving mesoporous silica-based materials modified with transition metals such as Ti, Cr, Co, Fe, and Ni to induce AO7 degradation through photocatalysis, show that bimetallic photocatalysts based on Mn and Ti exhibit large activity in azo dye remotion. Out of the previously studied materials, only bimetallic Cr and Ti-modified MCM-41 and SBA-15 materials exhibited a better response as a photocatalyst, although the presence of hexavalent Cr poses a significant drawback due to its high toxicity and potential leaching into the liquid phase [16,51]. Another silica-based material prepared as a mixed Si-Nb oxide achieved similar removal amounts to those of this study in 180 min of light exposure, but employing a lamp with an emission light

peaking in the UVB range, in addition to relying on niobium, a much rarer and more expensive metal than manganese and titanium [53]. Among non-silica-based materials, mesoporous anatase modified with Mo exhibits much reduced AO7 removal numbers when exposed to a 400 nm light source compared to activity at 365 nm in the same time lapse [54]. Even more diminished numbers are reported for photocatalysts based on Ag-modified ZnO [55], with around 40% of AO7 removal under exposure to 400 nm light for 180 min. Therefore, Mo and particularly Ag do not demonstrate being very effective at shifting the absorbance peak from the semiconductors to wavelengths in the UV–visible border. Low AO7 removal numbers (approximately 40%) are observed for Ni-modified $TiO_2$ bilayer films intermittently exposed to 365 nm light for four hours in an eight-hour process [56]. It must also be added that one of the main benefits from these Mn and Ti-based materials is the easy synthesis and modification process. Other photocatalysts with promising performance in AO7 removal, such as Bi-doped $SrTiO_3$ perovskites [57] and $Co_{78}Si_8B_{14}$/g-$C_3N_4$ nanocomposites [58], require highly-controlled synthesis processes at temperatures above 1000 °C, making them very energetically demanding and less practical.

As Ti/Mn/M proved to be the material with the highest photoactivity for AO7 removal, it was further studied. Materials synthesized with different Mn loads and calcined using two different heating rates were systematically evaluated to elucidate the selectivity towards ROS generation and correlate it with the synthesis conditions.

Figure 5 shows the results of the photocatalytic evaluation of the Ti/Mn(x)/M R(y) materials. The Ti/Mn(x)/M R4 materials show an AO7 removal activity that remains essentially independent of the Mn load on the material. On the other hand, Ti/Mn(2.5%)/M R8 is the material that shows the highest photoactivity, achieving AO7 removal close to 90%. However, as Mn load increases for Ti/Mn(x)/M R8 materials, AO7 degradation capacity becomes lower, remaining constant for 5 and 10 wt.% loads. Thus, a higher dispersion of more isolated Mn species would seem to favor the catalytic activity.

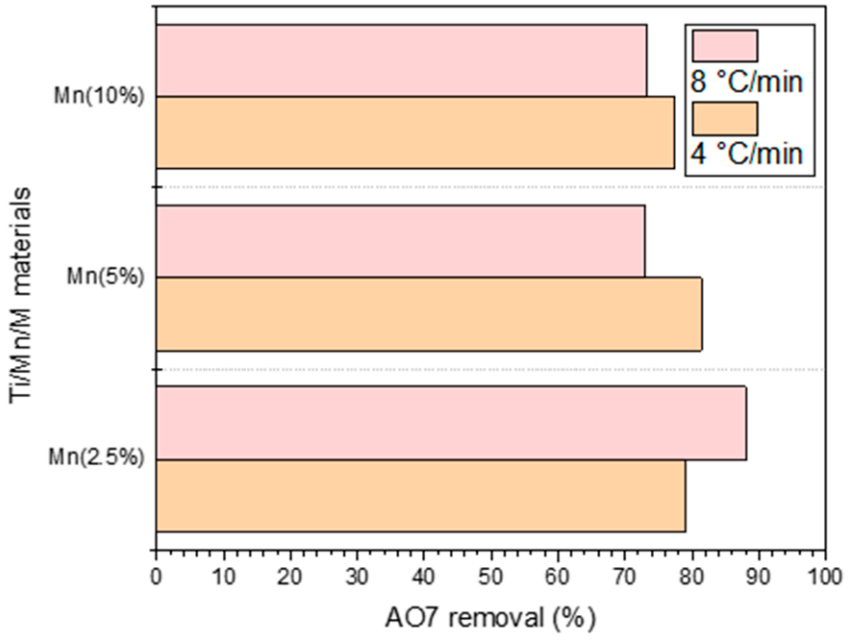


**Figure 5.** Comparison of AO7 degradation (%) after 180 min of photocatalytic activity for Ti/Mn(x)/M R(y) materials. Reaction conditions: pH = 5, T = 25 °C, catalyst concentration = 1 g/L, rotational speed = 600 rpm.

It is well established that the degradation of AO7 dye is primarily driven by reactive oxygen species (ROS) generated by photocatalytic materials [59–62]. To elucidate the predominant ROS involved in the degradation process, Ti/Mn(x)/M R(y) materials were

retested under the presence of different radical scavengers. Isopropanol was used as a hydroxyl radical scavenger, while chloroform acted as a superoxide radical scavenger, allowing for the selective inhibition of these radicals and enabling the assessment of their contributions to the AO7 degradation process. The results from these experiments are shown in Figure 6. The Ti/Mn(x)/M R4 materials (Figure 6A) exhibit a significant reduction in their AO7 degradation capacity in the presence of organic solvents. Notably, this decrease in photoactivity is particularly pronounced for the Ti/Mn(10%)/M R4 sample, where the degradation performance is similarly reduced in the presence of both isopropanol and chloroform. Thus, it can be inferred that Ti/Mn(x)/M R4 materials produce both hydroxyl and superoxide radicals, though it is only in the Ti/Mn(10%)/M R4 case that superoxide radicals are as active in AO7 degradation as hydroxyl radicals. On the other hand, Ti/Mn(x)/M R8 materials (Figure 6B) show a remarkable reduction of their AO7 removal capacity under aqueous isopropanol solution when their Mn load is relatively low, whereas for Ti/Mn(10%)/M R8 the photoactivity is largely reduced with both isopropanol and chloroform aqueous solutions. From these results, it can be inferred that Ti/Mn(x)/M R8 materials show largely hydroxyl radical activity when Mn load is relatively low (2.5 and 5 wt.%). However, when the Mn load is increased to 10 wt.%, the contribution of the superoxide radical pathway in the degradation of AO7 significantly increases, becoming comparable to that of the hydroxyl radical pathway. These results confirm Mn as a successful dopant for ROS production, which is influenced by the metal content in the material and the calcination rate [63].

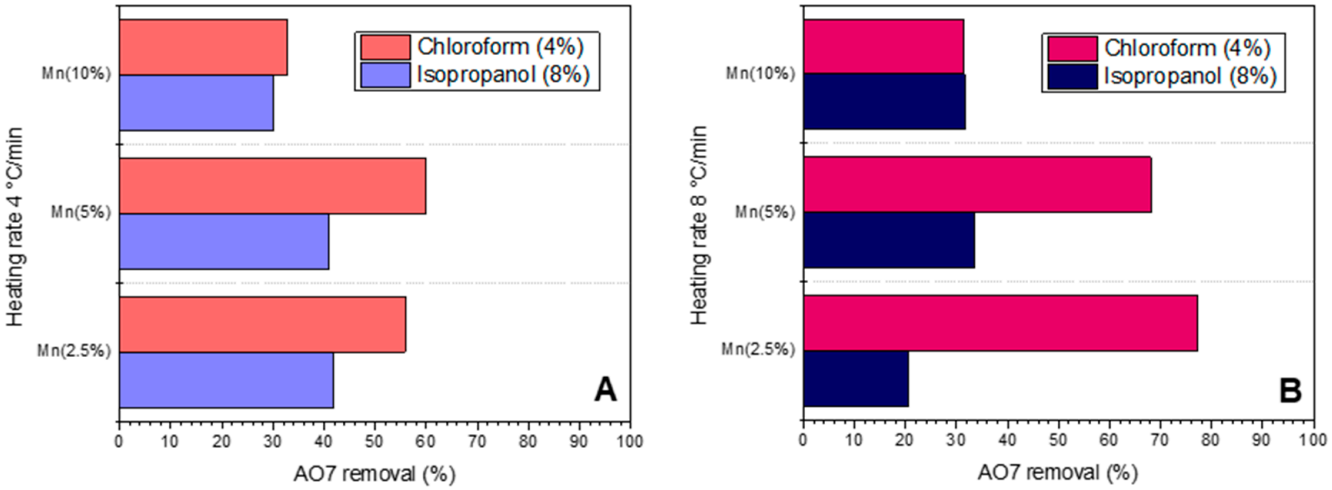


**Figure 6.** Comparison of AO7 degradation (%) after 180 min of photocatalytic activity for (**A**) Ti/Mn(x)/M R4 and (**B**) Ti/Mn(x)/M R8 materials. Reaction conditions: pH = 5, T = 25 °C, catalyst concentration = 1 g/L, rotational speed = 600 rpm.

Based on this, Ti/Mn(2.5%)/M R8 and Ti/Mn(10%)/M R8 were defined as the most and least photoactive materials, respectively. In order to study the superoxide radical generation and confirm that, according to the literature, they are generated through surface reduction of molecular oxygen with photoinduced electrons from the catalyst [3], a test insufflating $N_2$ to induce $O_2$ displacement was performed. As can be seen in Figure 7, Ti/Mn(10%)/M R8 shows a larger reduction of its AO7 degradation capacity when $N_2$ displaces $O_2$, which confirms the contribution of the superoxide radical pathway in this material, as seen in Figure 6.

In order to detect the generation of superoxide species on the materials' surface, aqueous suspensions of Ti/Mn(2.5%)/M R8 and Ti/Mn(10%)/M R8 were irradiated and analyzed by in situ testing with ATR–FTIR spectroscopy. As indicated in previous studies [64], a broad peak appears in the region between 900 and 1200 $cm^{-1}$, corresponding to

surface Ti-OO-stretching, thus the considered superoxide adsorbed on the catalyst surface. As seen in Figure 8, the signal for Ti/Mn(2.5%)/M R8 is stronger than for Ti/Mn(10%)/M R8, indicating a greater amount of superoxide adsorbed on the Ti/Mn(2.5%)/M R8 surface.

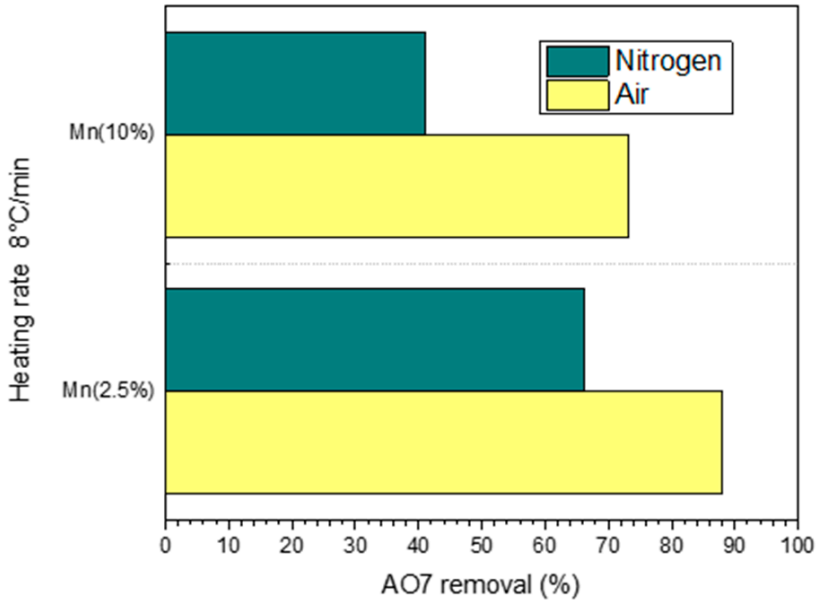


**Figure 7.** Comparison of AO7 degradation (%) after 180 min of photocatalytic activity for Ti/Mn(2.5%)/M R8 and Ti/Mn(10%)/M R8 materials under $N_2$ insufflation. Reaction conditions: pH = 5, T = 25 °C, catalyst concentration = 1 g/L, rotational speed = 600 rpm.

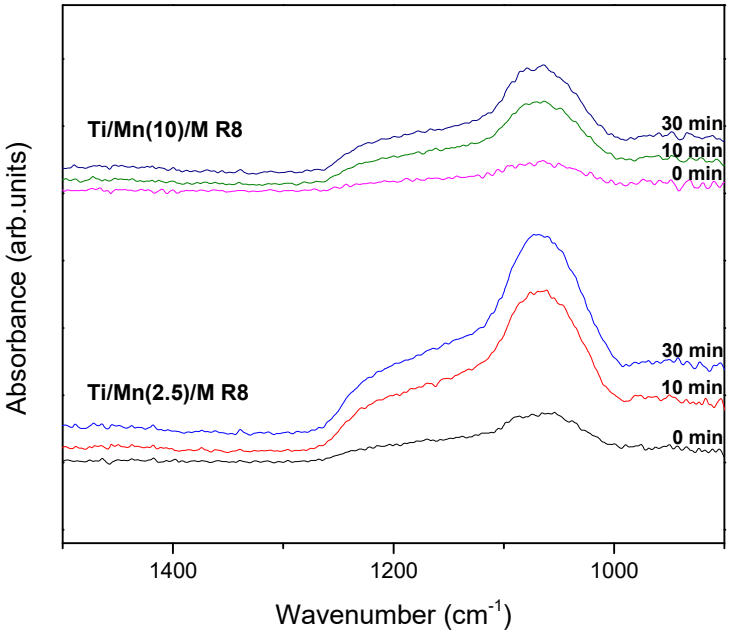


**Figure 8.** Attenuated total reflectance Fourier-transform infrared (ATR–FTIR) spectra (900–1500 $cm^{-1}$) for aqueous suspensions of Ti/Mn(2.5%)/M R8 and Ti/Mn(10%)/M R8 materials. Reaction conditions: pH = 5, T = 25 °C, catalyst concentration = 1 g/L.

In experiments using chloroform as a superoxide radical scavenger or with $N_2$ for oxygen displacement, Ti/Mn(10%)/M R8 exhibits higher superoxide radical activity in the degradation of AO7. This suggests that superoxide radicals are more readily released from the catalyst surface, resulting in a decrease in the peak corresponding to adsorbed superoxide on Ti/Mn(10%)/M R8 (Figure 8). Conversely, for Ti/Mn(2.5%)/M R8, the superoxide radicals remain attached to the catalyst surface for a longer period, which

would give them time to transform into hydrogen peroxide ($H_2O_2$) and subsequently into hydroxyl radicals (•OH), favoring AO7 degradation by this pathway [64].

### *3.3. Characterization of Mn Species in the Materials*

Considering the catalytic results, the solids were further characterized with the aim of deepening the analysis of the developed metallic species that produce the different catalytic activities and pathways observed for the Ti/Mn(x)/M R8 materials.

The XPS spectra in the O1s, Ti2p, and Mn2p regions for all Ti/Mn(x)/M R8 materials are presented in Figure 9.

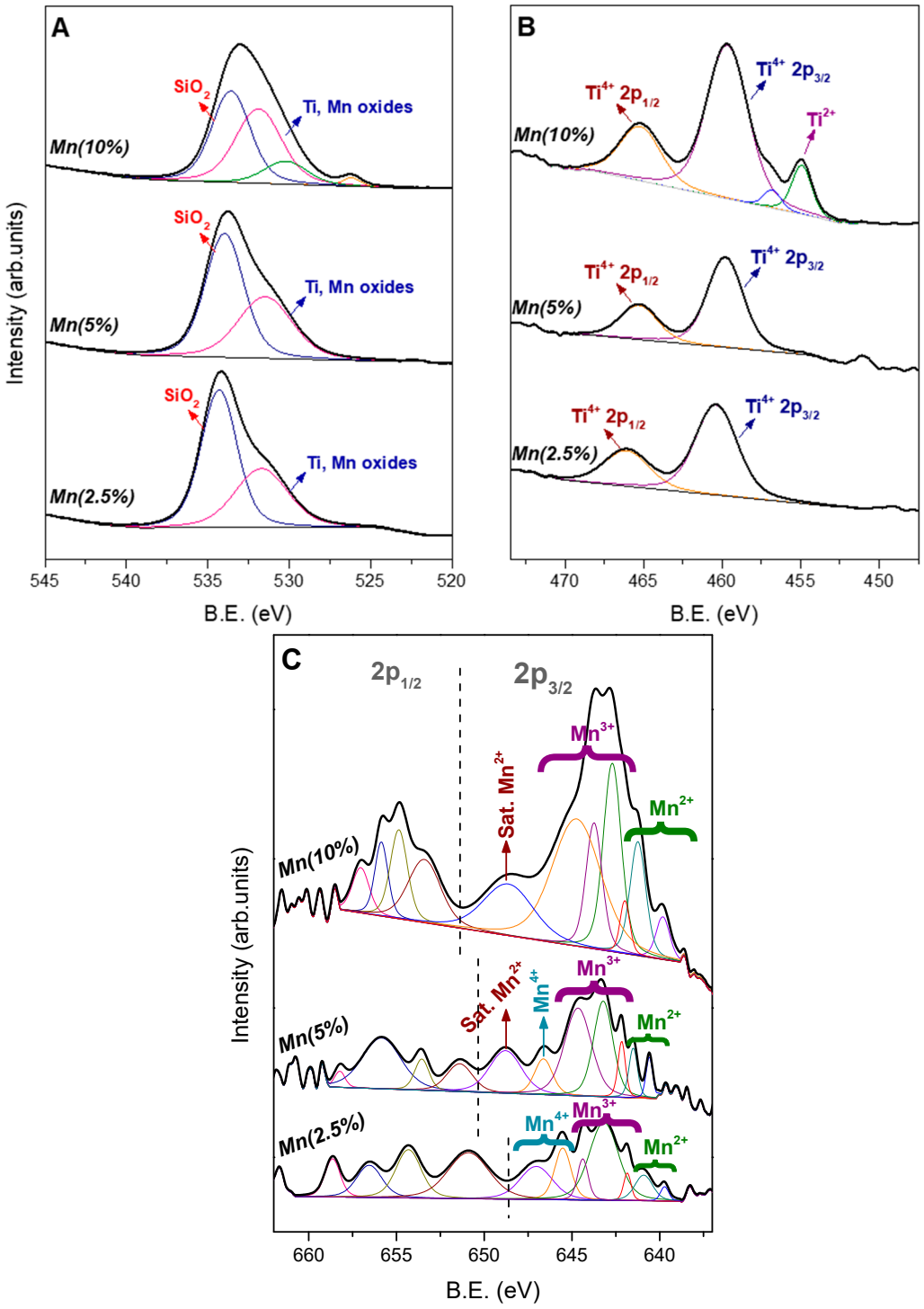


**Figure 9.** XPS spectra in the regions of (**A**) O1s, (**B**) Ti2p, and (**C**) Mn2p for Ti/Mn(x)/M R8 materials.

The O1s XPS spectra for all Ti/Mn(x)/M R8 materials (Figure 9A) show a peak at 533.58–534.31 eV, corresponding to $SiO_2$ species belonging to the mesoporous support [65], and one at 531.48–531.88 eV, corresponding to either Ti or Mn oxide species. These last species could not be distinguished from one another due to, according to the literature, their corresponding B.E. having very similar values [66,67]. Nonetheless, this peak increases along with Mn load, indicating the growing development of $MnO_x$ species on the solid surface. A small extra peak can be found in the case of Ti/Mn(10%)/M, which cannot be ascribed to metal oxides, but to a double charge effect due to its low binding energy [68,69]. Meanwhile, the Si 2p XPS spectra for all Ti/Mn(x)/M R8 materials are presented in Figure S4 (Supplementary Material). As it is shown, there is a series of intense signals at 103.73–104.43 eV, corresponding to Si-O-Si (siloxane) bonding, while another series of signals is shown between 100.7 and 102.8 eV, which is ascribed to Si-O-H (silanol) groups, confirming the presence of a silica framework [70].

As seen in the XPS spectra in the Ti2p region (Figure 9B), all Ti/Mn(x)/M R8 materials show peaks at 459.68–460.38 and 465.22–466.08 eV, corresponding to $Ti2p_{3/2}$ and $Ti2p_{1/2}$ in $Ti^{4+}$ species (despite peaks moving to higher B.E. values than those of pure oxides). At the same time, Ti/Mn(10%)/M R8 shows a peak at 454.93 eV, which corresponds to $Ti^{2+}$, as indicated by the literature [66]. It is evident that increased loadings of Mn modify the chemical environment of Ti.

In the Mn region (Figure 9C), an increase in signal intensity is observed with increasing Mn loading, which is consistent with the atomic percentage (At%) values obtained from XPS analysis. The Mn At% increases from 1.41% in Ti/Mn(2.5%)/M to 2.14% in Ti/Mn(5%)/M and reaches 4.17% in Ti/Mn(10%)/M. It should be noted that the "X" in Ti/Mn(X)/M refers to the nominal weight percentage, not the atomic percentage. As it can be seen in the spectra for three solids, a $Mn2p_{3/2}$ region can be identified at binding energy (B.E.) levels between 640 and 650 eV, approximately, along with a $Mn2p_{1/2}$ region between 650 and 660 eV. This delimitation is due to spin-orbit splitting and, as seen in the spectra, the $Mn2p_{1/2}$ region moves to higher B.E. values with higher Mn loadings. As expected from previous studies, a multiplet splitting is shown in the $Mn2p_{3/2}$ region [71–74]. These multiplet bands show different types of asymmetries as Mn load increases, indicating varying states of Mn species in the materials, with B.E. values similar to those of pure oxide species [67,72,73]. All Ti/Mn(x)/M R8 materials show low B.E. signals at 639.72–640.59 and 640.91–641.51 eV, corresponding to $Mn^{2+}$ species. The materials show also signals at 641.84–642.16, 643.18–643.74, and 644.38–644.73 eV, with an additional 642.70 eV peak in the case of Ti/Mn(10%)/M R8, all attributed to $Mn^{3+}$ species [67]. Ti/Mn(2.5%)/M R8 also shows signals at 645.52 and 647.04 eV, which can be attributed to $Mn^{4+}$ [67]. As Mn loading increases, these signals cannot be found anymore (only a peak at 646.62 eV appears in the case of Ti/Mn(5%)/M R8), while a $Mn^{2+}$ satellite peak formed due to a shake-up effect [71,74,75] can be traced at 648.63–648.78 eV. The high proportion of $Mn^{3+}$ species in Ti/Mn(x)/M R8 materials could give account for their considerable photocatalytic activity as indicated in previous studies [76].

The percentage area under the band for each Mn species identified in the XPS spectra is presented in Table 2. The results show that as the nominal Mn load increases, $Mn^{2+}$ and $Mn^{3+}$ species become predominant at the expense of $Mn^{4+}$. The higher presence of $Mn^{2+}$ species on the Ti-rich surface of Ti/Mn(10%)/M R8 can be linked to the enhanced superoxide radical activity, as $Mn^{2+}$ has been signaled as the electron donor for photogenerated holes in oxides of other transition metals [77].

**Table 2.** Percentage of area under the curve corresponding to each of the XPS-detected Mn species in the materials.

| Material | $Mn^{2+}$ (%) | $Mn^{3+}$ (%) | $Mn^{4+}$ (%) | Total (%) |
|---|---|---|---|---|
| Ti/Mn(2.5%)/M R8 | 10.67 | 53.72 | 35.61 | 100.00 |
| Ti/Mn(5%)/M R8 | 26.58 | 64.50 | 8.92 | 100.00 |
| Ti/Mn(10%)/M R8 | 29.02 | 70.98 | 0.00 | 100.00 |

On the other hand, $Mn^{3+}$ and $Mn^{4+}$ species can act effectively as hole traps by capturing electrons from water, thereby promoting $^{\bullet}OH$ generation through $H_2O$ oxidation; however, they are not efficient in promoting $O_2^{\bullet-}$ production [78,79]. In systems with low Mn content (Ti/Mn(2.5%)/M R8), the percentage of $Mn^{3+}$ and $Mn^{4+}$ significantly exceeds that of $Mn^{2+}$ (90%), favoring $^{\bullet}OH$ production. However, as the total theoretical Mn loading increases, the $Mn^{4+}$ species disappears, shifting the $Mn^{2+}$ ratio to approximately 30%, promoting $O_2^{\bullet-}$ generation.

The UV–Vis DRS spectra of the Ti/Mn(x)/M R8 materials are shown in Figure 10A. Focusing on the spectra obtained between 200 and 500 nm, a remarkably lower photosensitivity of the solid is observed as Mn load decreases. The Eg for these materials are shown in Figure 10B, as calculated from the UV–Vis DR spectra. A band gap reduction from 3.42 eV for Ti/Mn(2.5%)/M R8 to 3.26 eV for Ti/Mn(10%)/M R8 is observed. These results are consistent with the types of ROS generated. Thus, as hydroxyl requires more energy to be generated [3,33,52,80], Ti/Mn(2.5%)/M R8, which presents the highest Eg, promotes its production.

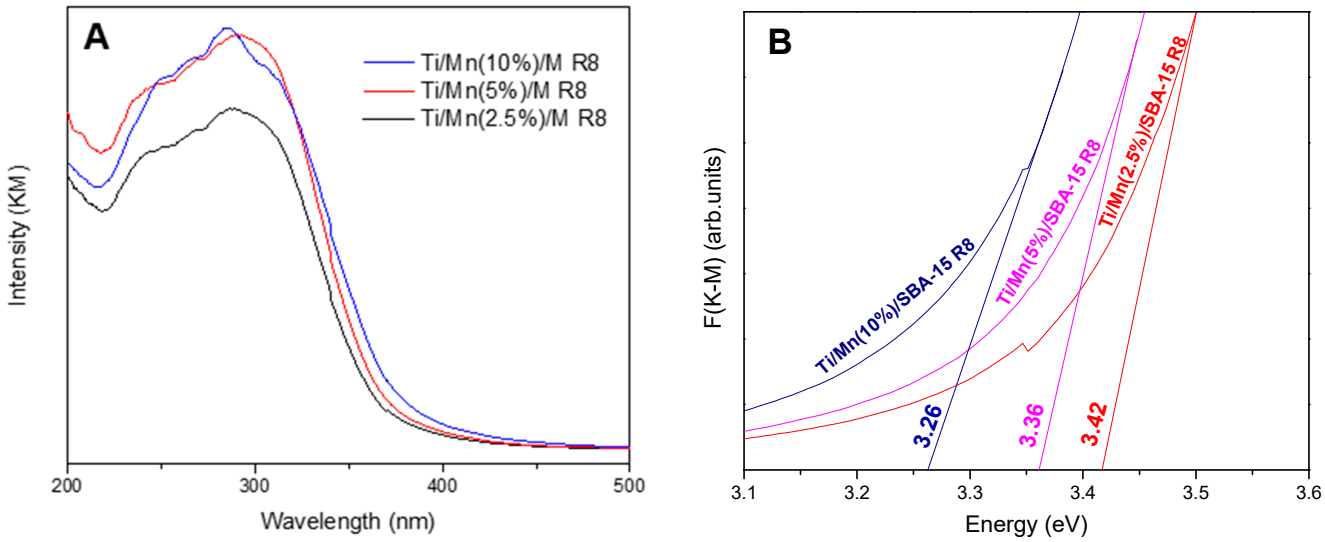


**Figure 10.** UV–Vis diffuse reflectance (DR) spectra of the synthesized Ti/Mn(X)/M R8 materials (**A**) and band gap estimation based on fitting Kubelka–Munk equation values as a function of the energy (**B**).

The Ti/Mn(10%)/M R8 material, by presenting a lower Eg, would not able to provide enough energy to generate $^{\bullet}OH$, but it could produce $O_2^{\bullet-}$, since these require less energy for their formation. This energy difference favors the selective formation of one type of radical over the other [33,52].

## 4. Conclusions

Bimetallic photocatalysts based on the dispersion of Ti/Cu, Ti/Co, and Ti/Mn metal couples onto a mesoporous silica with an SBA-15-like structure were successfully synthesized. The Ti/Mn couple was the most effective in photocatalytically degrading the model

dye AO7. For this reason, Mn was selected to vary and optimize the synthesis conditions (metal loading and heating rate during the calcination process) of the photocatalyst. Spectroscopic analysis revealed the presence of $Mn^{2+}$, $Mn^{3+}$, and $Mn^{4+}$ species in the different Ti/Mn materials, which could be associated with the generation of different reactive oxygen species (ROS) responsible for dye degradation. It was determined that lower Mn content (Ti/Mn(2.5%)/M R8) leads to materials with higher proportion of $Mn^{3+}$ and $Mn^{4+}$ species, which highly favor the generation of hydroxyl radicals ($^{\bullet}OH$). Conversely, at higher Mn loadings (Ti/Mn(10%)/M), the $Mn^{2+}$ species becomes more prevalent, reducing the band gap energy and making superoxide radical production by electron transfer feasible. Moreover, since the energy required for superoxide radical formation is lower, this pathway is favored, increasing the generation of these radicals.

These results demonstrate how fine-tuning the synthesis parameters enables the development of optimized photocatalysts tailored for the selective production of specific radical species.

**Supplementary Materials:** The following supporting information can be downloaded at: https://www.mdpi.com/article/10.3390/suschem6040031/s1, Figure S1. AO7 amount within 180 min of light exposure in the absence of a photocatalyst. Reaction conditions: pH = 5, T = 25 °C, rotational speed = 600 rpm; Figure S2. Low-angle X-ray diffraction (XRD) pattern of different modified and unmodified silica frameworks. The diffractograms were smoothed to reduce baseline noise and distinguish the peaks assigned to planes (110) and (200); Figure S3. UV–Vis diffuse reflectance (DR) spectra of the synthesized Ti/M, Ti/Co/M, Ti/Cu/M, and Ti/Mn/M materials (A) and band gap estimation based on fitting Kubelka–Munk equation values as a function of the energy (B); Figure S4. XPS spectra in the regions of Si2p for Ti/Mn(x)/M R8 materials.

**Author Contributions:** Conceptualization, G.A.E. and G.O.F.; methodology, F.E.V., V.R.E. and G.O.F.; validation, F.E.V., V.R.E. and G.O.F.; formal analysis, F.E.V. and G.O.F.; investigation, F.E.V.; resources, T.B.B. and G.F.G.; writing—original draft preparation, F.E.V.; writing—review and editing, T.B.B., V.R.E., G.A.E. and G.O.F.; visualization, F.E.V.; supervision, G.O.F.; project administration, G.A.E.; funding acquisition, G.F.G. and G.O.F. All authors have read and agreed to the published version of the manuscript.

**Funding:** This research was funded by Agencia Nacional de Promoción de la Investigación, el Desarrollo Tecnológico y la Innovación through the PICT-2021-GRFTI Project No. 00568 project and European Commission through H2020-MSCARISE-2020-NESTOR Project No. 101007629.

**Institutional Review Board Statement:** Not applicable.

**Informed Consent Statement:** Not applicable.

**Data Availability Statement:** The original contributions presented in this study are included in the article and in Supplementary Materials. Further inquiries can be directed to the corresponding author.

**Acknowledgments:** F.E.V., V.R.E., T.B.B., G.A.E. and G.O.F. are members of CONICET. The authors are grateful to CONICET, UTN, and H2020-MSCARISE-2020-NESTOR PROJECT No. 101007629 for the financial support.

**Conflicts of Interest:** The authors declare no conflicts of interest. The funders had no role in the design of the study; in the collection, analyses, or interpretation of data; in the writing of the manuscript; or in the decision to publish the results.

## Abbreviations

The following abbreviations are used in this manuscript:

| | |
|---|---|
| XPS | X-ray photoelectronic spectroscopy |
| UV–Vis | Ultraviolet and visible electromagnetic waves |
| DRS | Diffuse reflectance spectroscopy |

| | |
|---|---|
| AOP | Advanced oxidation processes |
| ROS | Reactive oxygen species |
| AO7 | Acid Orange 7 |
| TEOS | Tetraethoxysilane |
| XRD | X-ray diffraction |
| LED | Light-emitting diode |
| ATR-FTIR | Attenuated Total Reflectance–Fourier-Transform Infrared |
| BET | Brunauer–Emmett–Teller |
| PV | Pore volume |
| PD | Pore diameter |
| DR | Diffuse reflectance |
| KM | Kubelka–Munk |
| Eg | Band gap energy |

## References


1. Wang, J.; Wang, S. Reactive Species in Advanced Oxidation Processes: Formation, Identification and Reaction Mechanism. *Chem. Eng. J.* **2020**, *401*, 126158. [CrossRef]
2. Yuan, S.; Wang, M.; Liu, J.; Guo, B. Recent Advances of SBA-15-Based Composites as the Heterogeneous Catalysts in Water Decontamination: A Mini-Review. *J. Environ. Manag.* **2020**, *254*, 109787. [CrossRef]
3. Nosaka, Y.; Nosaka, A.Y. Generation and Detection of Reactive Oxygen Species in Photocatalysis. *Chem. Rev.* **2017**, *117*, 11302–11336. [CrossRef]
4. Rayaroth, M.P.; Aravindakumar, C.T.; Shah, N.S.; Boczkaj, G. Advanced Oxidation Processes (AOPs) Based Wastewater Treatment—Unexpected Nitration Side Reactions—A Serious Environmental Issue: A Review. *Chem. Eng. J.* **2022**, *430*, 133002. [CrossRef]
5. Rouster, P.; Pavlovic, M.; Szilagyi, I. Immobilization of Superoxide Dismutase on Polyelectrolyte-Functionalized Titania Nanosheets. *ChemBioChem* **2018**, *19*, 404–410. [CrossRef]
6. Nazarewicz, R.R.; Bikineyeva, A.; Dikalov, S.I. Rapid and Specific Measurements of Superoxide Using Fluorescence Spectroscopy. *J. Biomol. Screen.* **2013**, *18*, 498–503. [CrossRef]
7. Liu, R.H.; Fu, S.Y.; Zhan, H.Y.; Lucia, L.A. General Spectroscopic Protocol to Obtain the Concentration of the Superoxide Anion Radical. *Ind. Eng. Chem. Res.* **2009**, *48*, 9331–9334. [CrossRef]
8. Parrino, F.; Livraghi, S.; Giamello, E.; Ceccato, R.; Palmisano, L. Role of Hydroxyl, Superoxide, and Nitrate Radicals on the Fate of Bromide Ions in Photocatalytic $TiO_2$ Suspensions. *ACS Catal.* **2020**, *10*, 7922–7931. [CrossRef]
9. Gülçin, I.; Huyut, Z.; Elmastaş, M.; Aboul-Enein, H.Y. Radical Scavenging and Antioxidant Activity of Tannic Acid. *Arab. J. Chem.* **2010**, *3*, 43–53. [CrossRef]
10. Mohammad, M.; Khan, A.Y.; Subhani, M.S.; Bibi, N.; Ahmad, S.; Saleemi, S. Kinetics and Electrochemical Studies on Superoxide. *Res. Chem. Intermed.* **2001**, *27*, 259–267. [CrossRef]
11. Hayyan, M.; Hashim, M.A.; Alnashef, I.M. Superoxide Ion: Generation and Chemical Implications. *Chem. Rev.* **2016**, *116*, 3029–3085. [CrossRef]
12. Bartosz, G. Use of Spectroscopic Probes for Detection of Reactive Oxygen Species. *Clin. Chim. Acta* **2006**, *368*, 53–76. [CrossRef]
13. Burns, J.M.; Cooper, W.J.; Ferry, J.L.; King, D.W.; DiMento, B.P.; McNeill, K.; Miller, C.J.; Miller, W.L.; Peake, B.M.; Rusak, S.A.; et al. Methods for Reactive Oxygen Species (ROS) Detection in Aqueous Environments. *Aquat. Sci.* **2012**, *74*, 683–734. [CrossRef]
14. Choi, H.S.; Kim, J.W.; Cha, Y.-N.; Kim, C. A Quantitative Nitroblue Tetrazolium Assay for Determining Intracellular Superoxide Anion Production in Phagocytic Cells. *J. Immunoass. Immunochem.* **2006**, *27*, 31–44. [CrossRef]
15. Anastasescu, C.; Negrila, C.; Angelescu, D.G.; Atkinson, I.; Anastasescu, M.; Spataru, N.; Zaharescu, M.; Balint, I. Particularities of Photocatalysis and Formation of Reactive Oxygen Species on Insulators and Semiconductors: Cases of $SiO_2$, $TiO_2$ and Their Composite $SiO_2$-$TiO_2$. *Catal. Sci. Technol.* **2018**, *8*, 5657–5668. [CrossRef]
16. Elías, V.R.; Ferrero, G.O.; Oliveira, R.G.; Eimer, G.A. Improved Stability in SBA-15 Mesoporous Materials as Catalysts for Photo-Degradation Processes. *Microporous Mesoporous Mater.* **2016**, *236*, 218–227. [CrossRef]
17. Liou, T.H.; Liu, R.T.; Liao, Y.C.; Ku, C.E. Green and Sustainable Synthesis of Mesoporous Silica from Agricultural Biowaste and Functionalized with $TiO_2$ Nanoparticles for Highly Photoactive Performance. *Arab. J. Chem.* **2024**, *17*, 105764. [CrossRef]
18. Bai, H.; Li, X.; Hu, C.; Zhang, X.; Li, J.; Yan, Y.; Xi, G. Large-Scale, Three-Dimensional, Free-Standing, and Mesoporous Metal Oxide Networks for High-Performance Photocatalysis. *Sci. Rep.* **2013**, *3*, 2204. [CrossRef] [PubMed]
19. Grant, J.T.; Carrero, C.A.; Love, A.M.; Verel, R.; Hermans, I. Enhanced Two-Dimensional Dispersion of Group v Metal Oxides on Silica. *ACS Catal.* **2015**, *5*, 5787–5793. [CrossRef]

20. Wahba, M.A.; Khaled, R.K.; Dawy, M. Tailored Bimetallic Zn/Ni and Zn/Ag MCM-41 Photocatalysts for Enhanced Visible-Light Photocatalytic Tetracycline Degradation. *Sci. Rep.* **2025**, *15*, 5725. [CrossRef]
21. Wang, M.; Yang, L.; Guo, C.; Liu, X.; He, L.; Song, Y.; Zhang, Q.; Qu, X.; Zhang, H.; Zhang, Z.; et al. Bimetallic Fe/Ti-Based Metal–Organic Framework for Persulfate-Assisted Visible Light Photocatalytic Degradation of Orange II. *ChemistrySelect* **2018**, *3*, 3664–3674. [CrossRef]
22. Khandekar, D.C.; Bhattacharyya, A.R.; Bandyopadhyaya, R. Role of Impregnated Nano-Photocatalyst ($Sn_xTi_{(1-x)}O_2$) inside Mesoporous Silica (SBA-15) for Degradation of Organic Pollutant (Rhodamine B) under UV Light. *J. Environ. Chem. Eng.* **2019**, *7*, 103433. [CrossRef]
23. Shoneye, A.; Jiao, H.; Tang, J. Bimetallic $FeO_x$-$MO_x$ Loaded $TiO_2$ (M = Cu, Co) Nanocomposite Photocatalysts for Complete Mineralization of Herbicides. *J. Phys. Chem. C* **2023**, *127*, 1388–1396. [CrossRef]
24. Bharati, B.; Mishra, N.C.; Sinha, A.S.K.; Rath, C. Unusual Structural Transformation and Photocatalytic Activity of Mn Doped TiO2 Nanoparticles under Sunlight. *Mater. Res. Bull.* **2020**, *123*, 110710. [CrossRef]
25. Čižmar, T.; Lavrenčič Štangar, U.; Fanetti, M.; Arčon, I. Effects of Different Copper Loadings on the Photocatalytic Activity of $TiO_2$-$SiO_2$ Prepared at a Low Temperature for the Oxidation of Organic Pollutants in Water. *ChemCatChem* **2018**, *10*, 2982–2993. [CrossRef]
26. Ullrich, A.; Rahman, M.M.; Azhar, A.; Kühn, M.; Albrecht, M. Synthesis of Iron Oxide Nanoparticles by Decomposition of Iron-Oleate: Influence of the Heating Rate on the Particle Size. *J. Nanoparticle Res.* **2022**, *24*, 183. [CrossRef]
27. Ristig, S.; Cibura, N.; Strunk, J. Manganese Oxides in Heterogeneous (Photo)Catalysis: Possibilities and Challenges. *Green* **2015**, *5*, 23–41. [CrossRef]
28. Bhattacharyya, K.; Mane, G.P.; Rane, V.; Tripathi, A.K.; Tyagi, A.K. Selective $CO_2$ Photoreduction with Cu-Doped $TiO_2$ Photocatalyst: Delineating the Crucial Role of Cu-Oxidation State and Oxygen Vacancies. *J. Phys. Chem. C* **2021**, *125*, 1793–1810. [CrossRef]
29. Adamu, A.; Isaacs, M.; Boodhoo, K.; Abegão, F.R. Investigation of Cu/TiO2 Synthesis Methods and Conditions for $CO_2$ Photocatalytic Reduction via Conversion of Bicarbonate/Carbonate to Formate. *J. $CO_2$ Util.* **2023**, *70*, 102428. [CrossRef]
30. Liyanaarachchi, H.; Thambiliyagodage, C.; Liyanaarachchi, C.; Samarakoon, U. Efficient Photocatalysis of Cu Doped $TiO_2$/g-$C_3N_4$ for the Photodegradation of Methylene Blue. *Arab. J. Chem.* **2023**, *16*, 104749. [CrossRef]
31. Eldoma, M.A.; Alaswad, S.O.; Mahmoud, M.A.; Qudsieh, I.Y.; Hassan, M.; Bakather, O.Y.; Elawadi, G.A.; Abouatiaa, A.F.F.; Alomar, M.S.; Elhassan, M.S.; et al. Enhancing Photocatalytic Performance of Co-$TiO_2$ and Mo-$TiO_2$-Based Catalysts through Defect Engineering and Doping: A Study on the Degradation of Organic Pollutants under UV Light. *J. Photochem. Photobiol. A Chem.* **2024**, *446*, 115164. [CrossRef]
32. Kunnamareddy, M.; Ganesan, S.; Hatamleh, A.A.; Alnafisi, B.K.; Rajendran, R.; Chinnasamy, R.; Arumugam, P.; Diravidamani, B.; Lo, H.M. Enhancement in the Visible Light Induced Photocatalytic and Antibacterial Properties of Titanium Dioxide Codoped with Cobalt and Sulfur. *Environ. Res.* **2023**, *216*, 114705. [CrossRef]
33. Viale, F.E.; Winkler, E.L.; Lima, E.; Goya, G.F.; Benzaquén, T.B.; Elías, V.R.; Eimer, G.A.; Ferrero, G.O. Optimization of Photocatalytic Activity in Transition Metal-Modified Mesoporous Silicas: Fine-Tuning Properties to Elucidate Radical Reaction Pathways by EPR. *J. Mater. Chem. C Mater.* **2025**, *13*, 12440–12450. [CrossRef]
34. Goto, H.; Hanada, Y.; Ohno, T.; Matsumura, M. Quantitative Analysis of Superoxide Ion and Hydrogen Peroxide Produced from Molecular Oxygen on Photoirradiated $TiO_2$ Particles. *J. Catal.* **2004**, *225*, 223–229. [CrossRef]
35. Šihor, M.; Reli, M.; Vaštyl, M.; Hrádková, K.; Matějová, L.; Kočí, K. Photocatalytic Oxidation of Methyl Tert-Butyl Ether in Presence of Various Phase Compositions of $TiO_2$. *Catalysts* **2020**, *10*, 35. [CrossRef]
36. Zhao, D.; Feng, J.; Huo, Q.; Melosh, N.; Fredrickson, G.H.; Chmelka, B.F.; Stucky, G.D. Triblock Copolymer Syntheses of Mesoporous Silica with Periodic 50 to 300 Angstrom Pores. *Science* **1998**, *279*, 548–552. [CrossRef]
37. Intelligent LED Solutions. *T9090 1 PowerStar UV, ILH-XU01-Sxxx-SC211-WIR200 Datasheet*; Intelligent LED Solutions: Thatcham, UK, 2017.
38. Taiwan Semiconductor Lighting Corporation. *T9090U-UNL1 High Power UV LED. T9090U-UNL1 Series Product Datasheet*; Taiwan Semiconductor Lighting Corporation: Zhunan, Taiwan, 2017.
39. Thommes, M.; Kaneko, K.; Neimark, A.V.; Olivier, J.P.; Rodriguez-Reinoso, F.; Rouquerol, J.; Sing, K.S.W. Physisorption of Gases, with Special Reference to the Evaluation of Surface Area and Pore Size Distribution (IUPAC Technical Report). *Pure Appl. Chem.* **2015**, *87*, 1051–1069. [CrossRef]
40. Janus, R.; Wądrzyk, M.; Lewandowski, M.; Natkański, P.; Łątka, P.; Kuśtrowski, P. Understanding Porous Structure of SBA-15 upon Pseudomorphic Transformation into MCM-41: Non-Direct Investigation by Carbon Replication. *J. Ind. Eng. Chem.* **2020**, *92*, 131–144. [CrossRef]
41. Villarroel Rocha, J.; Barrera, D.; Sapag, K. Improvement in the Pore Size Distribution for Ordered Mesoporous Materials with Cylindrical and Spherical Pores Using the Kelvin Equation. *Top. Catal.* **2011**, *54*, 121–134. [CrossRef]

42. Trejda, M.; Drobnik, M.; Nurwita, A. Application of Microwave Radiation in the Grafting of Acidic Sites on SBA-15 Type Material. *J. Porous Mater.* **2021**, *28*, 1261–1267. [CrossRef]
43. Nurwita, A.; Trejda, M. The Effect of Mesoporous Structure of the Support on the Oxidation of Dibenzothiophene. *Int. J. Mol. Sci.* **2023**, *24*, 16597. [CrossRef]
44. Cychosz, K.A.; Thommes, M. Progress in the Physisorption Characterization of Nanoporous Gas Storage Materials. *Engineering* **2018**, *4*, 559–566. [CrossRef]
45. Mikolei, J.J.; Richter, D.; Pardehkhorram, R.; Helbrecht, C.; Schabel, S.; Meckel, T.; Biesalski, M.; Ceolin, M.; Andrieu-Brunsen, A. Nanoscale Pores Introduced into Paper via Mesoporous Silica Coatings Using Sol-Gel Chemistry. *Nanoscale* **2023**, *15*, 9094–9105. [CrossRef]
46. Gómez-Ruiz, S.; García-Peñas, A.; Prashar, S.; Rodríguez-Diéguez, A.; Fischer-Fodor, E. Anticancer Applications of Nanostructured Silica-Based Materials Functionalized with Titanocene Derivatives: Induction of Cell Death Mechanism through TNFR1 Modulation. *Materials* **2018**, *11*, 224. [CrossRef]
47. Colmenares-Zerpa, J.; Chimentão, R.J.; Gispert-Guirado, F.; Peixoto, A.F.; Llorca, J. Preparation of SBA-15 and Zr-SBA-15 Materials by Direct-Synthesis and PH-Adjustment Methods. *Mater. Lett.* **2021**, *301*, 130326. [CrossRef]
48. Gonçalves, N.P.F.; Paganini, M.C.; Armillotta, P.; Cerrato, E.; Calza, P. The Effect of Cobalt Doping on the Efficiency of Semiconductor Oxides in the Photocatalytic Water Remediation. *J. Environ. Chem. Eng.* **2019**, *7*, 103475. [CrossRef]
49. Pradhan, D.; Falletta, E.; Dash, S.K. Enhanced and Rapid Photocatalytic Degradation of Toxic Dyes by Cobalt Oxide and Modified Cobalt Oxide under Solar Light Irradiation. *Opt. Mater.* **2023**, *135*, 113368. [CrossRef]
50. Dong, G.; Hu, H.; Huang, X.; Zhang, Y.; Bi, Y. Rapid Activation of $Co_3O_4$ Cocatalysts with Oxygen Vacancies on $TiO_2$ Photoanodes for Efficient Water Splitting. *J. Mater. Chem. A Mater.* **2018**, *6*, 21003–21009. [CrossRef]
51. Elías, V.; Vaschetto, E.; Sapag, K.; Oliva, M.; Casuscelli, S.; Eimer, G. MCM-41-Based Materials for the Photo-Catalytic Degradation of Acid Orange 7. *Catal. Today* **2011**, *172*, 58–65. [CrossRef]
52. Xu, Y.; Schoonen, M.A.A. The Absolute Energy Positions of Conduction and Valence Bands of selected Semiconducting Minerals. *Am. Mineral.* **2000**, *85*, 543–556. [CrossRef]
53. Feliczak-Guzik, A.; Wawrzyńczak, A.; Nowak, I. Photocatalysis by Mixed Oxides Containing Niobium, Vanadium, Silica, or Tin. *Catalysts* **2025**, *15*, 118. [CrossRef]
54. Štengl, V.; Bakardjieva, S. Molybdenum-Doped Anatase and Its Extraordinary Photocatalytic Activity in the Degradation of Orange II in the UV and Vis Regions. *J. Phys. Chem. C* **2010**, *114*, 19308–19317. [CrossRef]
55. González-Rodríguez, J.; Fernández, L.; Bava, Y.B.; Buceta, D.; Vázquez-Vázquez, C.; López-Quintela, M.A.; Feijoo, G.; Moreira, M.T. Enhanced Photocatalytic Activity of Semiconductor Nanocomposites Doped with Ag Nanoclusters under UV and Visible Light. *Catalysts* **2020**, *10*, 31. [CrossRef]
56. Wongburapachart, C.; Pornaroontham, P.; Kim, K.; Rangsunvigit, P. Photocatalytic Degradation of Acid Orange 7 by NiO-$TiO_2$/$TiO_2$ Bilayer Film Photo-Chargeable Catalysts. *Coatings* **2023**, *13*, 141. [CrossRef]
57. Nunes, M.J.; Lopes, A.; Pacheco, M.J.; Ciríaco, L. Visible-Light-Driven AO7 Photocatalytic Degradation and Toxicity Removal at Bi-Doped SrTiO3. *Materials* **2022**, *15*, 2465. [CrossRef]
58. Yang, Z.; Ma, G.; Zhang, J. High-Efficiency Degradation of Orange II by $Co_{78}Si_8B_{14}$/g-$C_3N_4$ Composite Catalyst in a Visible-Light-Assisted Peroxymonosulfate Activation System. *Materials* **2025**, *18*, 1733. [CrossRef]
59. Biswas, B.D.; Datta, J.; Purkayastha, M.D.; Das, D.; Ray, P.P.; Dutta, A.; Majumder, T.P. Electrical and Photocatalytic Properties of Composites of Manganese and Titanium Oxides. *Surf. Interfaces* **2020**, *20*, 100606. [CrossRef]
60. Hafeez, M.; Afyaz, S.; Khalid, A.; Ahmad, P.; Khandaker, M.U.; Sahibzada, M.U.K.; Ahmad, I.; Khan, J.; Alhumaydhi, F.A.; Emran, T.B.; et al. Synthesis of Cobalt and Sulphur Doped Titanium Dioxide Photocatalysts for Environmental Applications. *J. King Saud. Univ. Sci.* **2022**, *34*, 102028. [CrossRef]
61. Kitchamsetti, N.; Didwal, P.N.; Mulani, S.R.; Patil, M.S.; Devan, R.S. Photocatalytic Activity of $MnTiO_3$ Perovskite Nanodiscs for the Removal of Organic Pollutants. *Heliyon* **2021**, *7*, e07297. [CrossRef]
62. Osgouei, M.S.; Khatamian, M.; Kakili, H. Improved Visible-Light Photocatalytic Activity of Mn3O4-Based Nanocomposites in Removal of Methyl Orange. *Mater. Chem. Phys.* **2020**, *239*, 122108. [CrossRef]
63. Wang, Y.; Lin, Y.; Zhang, J.; Gui, Y.; Liu, L. Enhanced Photocatalytic Performance of Mn-Doped $CeO_2$ Nanoribbons for VOCs Degradation: Investigating Charge Rearrangement and Local Electric Field Effects. *J. Environ. Chem. Eng.* **2023**, *11*, 111445. [CrossRef]
64. Kakuma, Y.; Nosaka, A.Y.; Nosaka, Y. Difference in $TiO_2$ Photocatalytic Mechanism between Rutile and Anatase Studied by the Detection of Active Oxygen and Surface Species in Water. *Phys. Chem. Chem. Phys.* **2015**, *17*, 18691–18698. [CrossRef]
65. Namiki, A.; Tanimoto, K.; Nakamura, T.; Ohtake, N.; Suzaki, T. XPS Study on the Early Stages of Oxidation of Si(100) by Atomic Oxygen. *Surf. Sci.* **1989**, *222*, 530–554. [CrossRef]
66. Biesinger, M.C.; Lau, L.W.M.; Gerson, A.R.; Smart, R.S.C. Resolving Surface Chemical States in XPS Analysis of First Row Transition Metals, Oxides and Hydroxides: Sc, Ti, V, Cu and Zn. *Appl. Surf. Sci.* **2010**, *257*, 887–898. [CrossRef]

67. Biesinger, M.C.; Payne, B.P.; Grosvenor, A.P.; Lau, L.W.M.; Gerson, A.R.; Smart, R.S.C. Resolving Surface Chemical States in XPS Analysis of First Row Transition Metals, Oxides and Hydroxides: Cr, Mn, Fe, Co and Ni. *Appl. Surf. Sci.* **2011**, *257*, 2717–2730. [CrossRef]
68. Kunthakudee, N.; Puangpetch, T.; Ramakul, P.; Serivalsatit, K.; Ponchio, C.; Hunsom, M. Ultra-Fast Green Synthesis of a Defective TiO2 Photocatalyst towards Hydrogen Production. *RSC Adv.* **2024**, *14*, 24213–24225. [CrossRef]
69. Fetisov, A.V.; Kozhina, G.A.; Estemirova, S.K.; Fetisov, V.B.; Gulyaeva, R.I. XPS Study of the Chemical Stability of $DyBa_2Cu_3O_{6+\delta}$ Superconductor. *Phys. C Supercond. Its Appl.* **2015**, *508*, 62–68. [CrossRef]
70. Paengjun, N.; Vibulyaseak, K.; Ogawa, M. Heterostructural Transformation of Mesoporous Silica–Titania Hybrids. *Sci. Rep.* **2021**, *11*, 3210. [CrossRef]
71. Ianhez-Pereira, C.; Onofre, Y.J.; Magon, C.J.; Rodrigues, A.d.G.; de Godoy, M.P.F. The Interplay between Mn Valence and the Optical Response of ZnMnO Thin Films. *Appl. Phys. A Mater. Sci. Process* **2020**, *126*, 337. [CrossRef]
72. Ilton, E.S.; Post, J.E.; Heaney, P.J.; Ling, F.T.; Kerisit, S.N. XPS Determination of Mn Oxidation States in Mn (Hydr)Oxides. *Appl. Surf. Sci.* **2016**, *366*, 475–485. [CrossRef]
73. Nesbitt, H.W.; Banerjee, D. Interpretation of XPS Mn(2p) Spectra of Mn Oxyhydroxides and Constraints on the Mechanism of MnO 2 Precipitation. *Am. Mineral.* **1998**, *83*, 305–315. [CrossRef]
74. Zhang, S.; Lv, J.; Han, R.; Wang, Z.; Christie, P.; Zhang, S. Sustained Production of Superoxide Radicals by Manganese Oxides under Ambient Dark Conditions. *Water Res.* **2021**, *196*, 117034. [CrossRef]
75. Xiong, Y.; Zhang, Y.; Zhou, C.; Yu, T. ROS Scavenging Manganese-Loaded Mesoporous Silica Nanozymes for Catalytic Anti-Inflammatory Therapy. *Adv. Powder Technol.* **2023**, *34*, 103886. [CrossRef]
76. Huang, J.; Zhong, S.; Dai, Y.; Liu, C.C.; Zhang, H. Effect of $MnO_2$ Phase Structure on the Oxidative Reactivity toward Bisphenol A Degradation. *Environ. Sci. Technol.* **2018**, *52*, 11309–11318. [CrossRef] [PubMed]
77. Jung, H.; Xu, X.; Wan, B.; Wang, Q.; Borkiewicz, O.J.; Li, Y.; Chen, H.; Lu, A.; Tang, Y. Photocatalytic Oxidation of Dissolved Mn(II) on Natural Iron Oxide Minerals. *Geochim. Cosmochim. Acta* **2021**, *312*, 343–356. [CrossRef]
78. Chen, M.; Zhang, J.; Yang, T.; Mao, S.; Zhao, H. Peroxymonosulfate Activation for Preferential Generation of Hydroxyl Radical with Atomic Mn Anchored $TiO_2$ in Photoelectrochemical Process. *Environ. Funct. Mater.* **2023**, *2*, 13–24. [CrossRef]
79. Nevárez-Martínez, M.C.; Kobylanski, M.P.; Mazierski, P.; Wółkiewicz, J.; Trykowski, G.; Malankowska, A.; Kozak, M.; Espinoza-Montero, P.J.; Zaleska-Medynska, A. Self-Organized $TiO_2$-$MnO_2$ Nanotube Arrays for Efficient Photocatalytic Degradation of Toluene. *Molecules* **2017**, *22*, 564. [CrossRef]
80. Cheeseman, S.; Christofferson, A.J.; Kariuki, R.; Cozzolino, D.; Daeneke, T.; Crawford, R.J.; Truong, V.K.; Chapman, J.; Elbourne, A. Antimicrobial Metal Nanomaterials: From Passive to Stimuli-Activated Applications. *Adv. Sci.* **2020**, *7*, 1902913. [CrossRef]